

Characterization and control of unconfined lateral diffusion under stencil masks

Zoltán Rácz and Alan Seabaugh^{a)}

Department of Electrical Engineering, University of Notre Dame, 266 Fitzpatrick Hall, Notre Dame, Indiana 46556

(Received 16 January 2007; accepted 12 April 2007; published 11 May 2007)

A quantitative study of the spreading behavior of electron-beam-evaporated Al, Au, Cr, Ge, Pt, and Ti on oxidized Si substrates has been performed using translated stencil masks. At least two mechanisms are needed to account for the lateral spreading of the deposited materials: The deposition edge moves by a Fickian diffusion with a diffusion coefficient of $6.7 \text{ nm}^2/\text{s}$ at 45°C which is approximately independent of the deposited material. Once under the stencil mask, the deposited material spreads $0.1\text{--}2 \mu\text{m}$ (at 45°C for under 2 h), in a thin layer as a result of surface diffusion. The evaporation in N_2 or O_2 at $50 \mu\text{Torr}$ significantly suppresses the spreading with Ti showing the greatest reduction of $(7\text{--}8)\times$.

© 2007 American Vacuum Society. [DOI: 10.1116/1.2737437]

I. INTRODUCTION

Nanofabrication techniques based on evaporation through translated^{1–4} or untranslated⁵ stencil masks enable patterned deposition of metals and dielectrics on surfaces uncontaminated by photoresists and solvents and free from attack by resist developers. Stencil masks are reconfigurable, since the same mask can be used with translation to define a wide variety of patterns. When dissimilar materials are alternately deposited through translated stencil apertures, differential etching can be used to remove one deposition with respect to another³ to form three-dimensional structures and nanoelectromechanical devices. Nanofabrication techniques using stencil masks require an understanding and control of the deposition profile.

Features formed by evaporation through stencil masks have an edge taper which is geometrically limited by the evaporator source size, source-to-substrate throw, and mask-to-substrate separation, and can be reduced to under 10 nm .^{1,3} A second factor affecting the edge profile is the reduction in the aperture size during deposition. The edge deposition depends on the material and is typically $1/3\text{--}1/6$ of the deposited layer thickness.¹ For a 20 nm thick deposition, the edge taper arising from clogging should also be under 10 nm . In this article, the edge profile of stencil mask depositions is examined and shown to be orders of magnitude greater than dictated by the geometrical edge taper or aperture clogging.

To compare the edge profiles of different materials the deposition substrate is mounted on a piezotranslation stage allowing the substrate to be translated to a clear area of the wafer between evaporations. This allows the direct comparison of deposition edge profiles for the same evaporation geometry, the same aperture, and the same wafer surface condition. In this study, the diffusive motion of materials on thermally oxidized Si surfaces near room temperature

(45°C) has been quantified for a wide range of evaporated materials including Al, Au, Cr, Ge, Pt, and Ti. This motion is shown to be driven by at least two mechanisms: a concentration-dependent diffusion process which governs the translation of the half-height of the deposited film and a surface diffusion process which feeds the growth of a thin surface layer under the stencil mask. This lateral surface diffusion is shown to be suppressed by the evaporation in oxygen and nitrogen background pressures.

Near room temperature the surface diffusion during evaporation through stencil apertures has been previously reported for several materials and substrates: Er and Au on oxidized Al and Si,¹ Sb and Si on Si (111),⁶ Al on Si, SiO_2 , and Si_3N_4 ,⁷ and Au on SiO_2 .⁸ However, a comparative study of the lateral spreading of a set of different materials on the same substrate during a single electron-beam deposition has not been previously performed. Atomic force microscopy (AFM) and scanning electron microscopy (SEM) are used to characterize the deposition profiles.

II. APPARATUS

The vacuum depositions were performed in an Airco/Temescal FC-1800 electron-beam evaporation system fitted with a subnanometer resolution Polytec PI P-731 x - y nanopositioner with built-in capacitive sensors and a closed-loop feedback controller. A custom mask-substrate fixture³ was constructed with interconnects to the controller via vacuum feedthroughs. The oxidized Si substrate is fixed to the wafer holder which is mounted on the flexure portion of the x - y stage. The stencil mask is placed in contact with the substrate to establish planarity and the mask holder is attached to the fixed portion of the x - y stage via three spacers that maintain a submillimeter gap between the stencil mask and the mask holder. Finally, the mask is fixed to the mask holder by a low-shrinkage, nonoutgassing polymer adhesive (Norland Optical Adhesive 63 by Norland Products Inc.). The apparatus is shielded from the radiative heat of the deposition sources by a 13-mm-thick stainless-steel plate located 25 cm

^{a)}Electronic mail: seabaugh.1@nd.edu

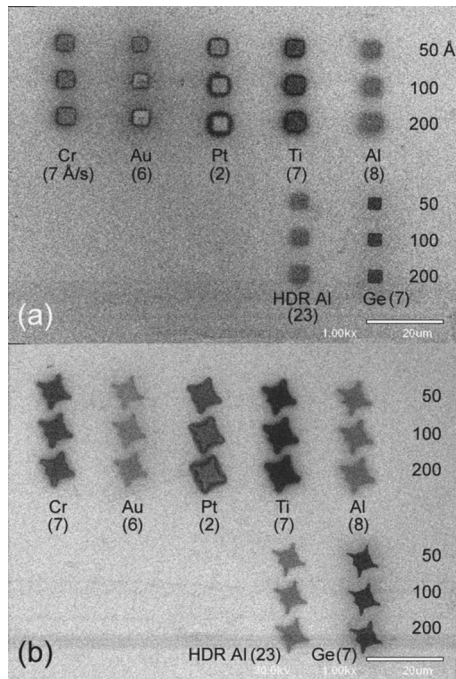


FIG. 1. Scanning electron micrograph of a sequence of depositions through the same stencil aperture which is translated between depositions: (a) approximately $3 \times 3 \mu\text{m}^2$ squares and (b) approximately $7 \mu\text{m}$ length star features. These two aperture openings were present on the same stencil mask. Deposition rates are given for each feature and for each material and three different deposition thicknesses were made as labeled on the right hand side of the micrograph. The order of the evaporations was from right to left by material and from thin to thick depositions. HDR means high deposition rate.

above the evaporation source. A closed-loop temperature controller driving a 1 kW quartz lamp is used to keep the mask holder at a constant temperature (45°C) during deposition to minimize the translation of the mask due to thermal expansion. The layer thicknesses and the deposition rates are measured by a crystal monitor.

III. EXPERIMENT

Silicon (100) substrates, 100 mm in diameter, were thermally oxidized at 1000°C for 360 min to grow an oxide with a thickness of approximately $1 \mu\text{m}$. A sequence of depositions of Al, Ti, Pt, Au, Cr, and Ge was executed through a KOH-etched Si mask with micron scale apertures.

Between depositions, the stencil mask was translated to a pristine area of the substrate by the piezoflexure stage.

The evaporations were performed under vacuum at 1.8×10^{-6} Torr with deposition rates in the range of $2\text{--}8 \text{ \AA}/\text{s}$. Aluminum was also evaporated at a high deposition rate (HDR) to see how rate affects the lateral spread. Figure 1 shows SEM images of the 21 depositions through two different apertures: a $3 \mu\text{m}$ square aperture in Fig. 1(a) and a $7 \mu\text{m}$ star aperture in Fig. 1(b). The star-shaped apertures form occasionally at lower KOH bath temperatures (78°C); because of the sharp angles, the difference between the lateral diffusion of different materials is amplified in the star patterns. For each material, three layer thicknesses were deposited: nominally 50, 100, and 200 \AA . The substrate was translated between each elemental deposition by $9 \mu\text{m}$ in the vertical direction in Fig. 1. After each deposition sequence (three depositions of the same material), the substrate was translated by $18 \mu\text{m}$ in the horizontal direction and the deposition sequence was repeated with a different element. The order of the depositions was right to left and top to bottom. The nominal thicknesses and deposition rates for each material are also indicated in Fig. 1.

IV. RESULTS AND DISCUSSION

The SEM micrographs of Fig. 1 show that the size and sharpness of the different deposited elements vary significantly even though they were deposited through the same aperture. This is especially apparent for the star structures of Fig. 1(b) where the Pt and Ti features are notably larger and less distinct (blurrier) than the Ge features. The examination of the thickness dependence for the same element shows that the lateral dimensions increase with increasing layer thicknesses.

AFM images of the deposited layers were obtained using a Digital Instruments multimode scanning probe microscope with a NanoScope IV controller in tapping mode with a resolution of $\leq 20 \text{ nm}$. Each of the images in Fig. 2 show a central bright square formed under the approximately $3 \mu\text{m}$ aperture. With the exception of Ge, each square is surrounded by a “halo” consisting of materials which spread out on the surface in a thin surface layer. The extent of this halo is different for each metal and increases with deposition thickness as previously noted from the SEM images. For Al, Ti, and Pt, the extent of the halo is between 0.9 and $2 \mu\text{m}$.

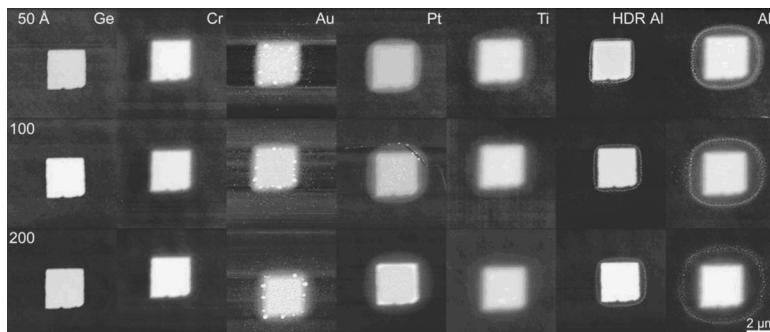


FIG. 2. Top-view atomic force microscope images of the deposited materials of Fig. 1.

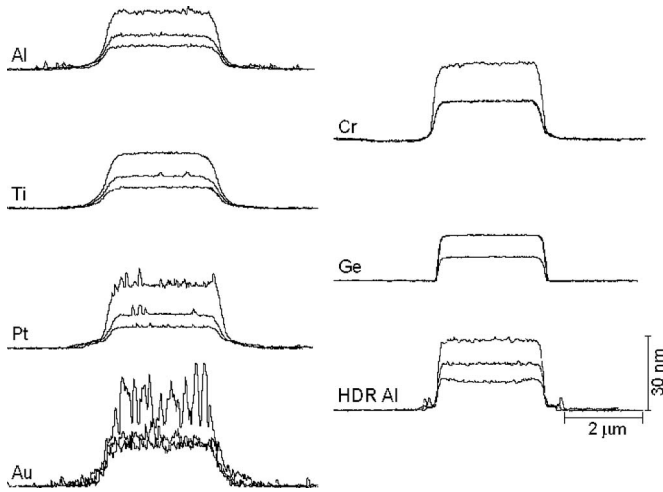


FIG. 3. Cross-sectional atomic force microscope line scans of the deposited structures grouped by element.

For Au, Al, and Pt, nanocrystalline features are also observed; for Au these are dispersed about the central-deposition square, while for Al the crystal formation begins about $1 \mu\text{m}$ from the deposition edge.

The lateral dimensions are compared by overlaying line scans from the AFM images (Fig. 3). The Au and Al microcrystal formations apparent in the AFM micrographs of Fig. 2 are also apparent in the line scans. The three nominal deposition thicknesses of 50, 100, and 200 \AA are overlaid for each element from which the actual thicknesses can be measured. Figure 4 compares the line scans of all the elements at the nominally 100 \AA thick deposition thickness. It is apparent that materials that produced a blurry SEM edge (Al, Ti, and Pt) have tapering sidewalls, while materials with well-defined SEM edges [Ge and high deposition rate (HDR) Al] have abrupt sidewalls.

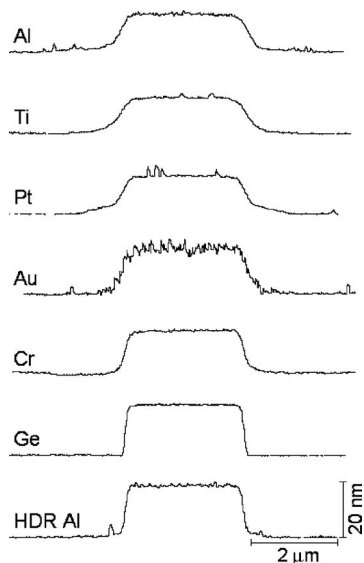


FIG. 4. Cross-sectional atomic force microscope line scans of depositions with 100 \AA nominal layer thickness.

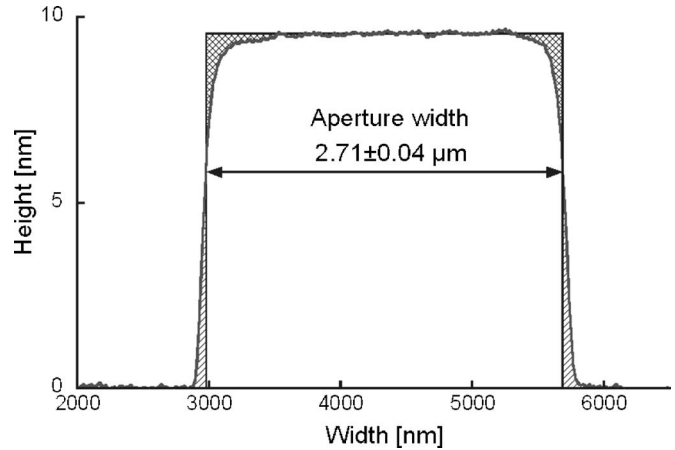


FIG. 5. Cross-sectional atomic force microscope image of the 95 \AA thick Ge deposition used to determine the size of the stencil mask aperture.

By determining the aperture size, the lateral spreading of all elements relative to the same stencil aperture can be directly measured. The principle of mass conservation is used to determine the deposition edge and estimate the aperture size.⁶ According to the SEM images, Ge is the least-diffusive element, therefore, the cross-sectional AFM image of the nominally 100 \AA thick Ge feature was used to estimate the aperture size (Fig. 5). The amount of Ge that moved under the stencil mask (hatched area) is set to be equal to the amount of material missing from the region of deposition (cross-hatched area).⁹ The equal mass point that defines the aperture edge and the size of the stencil mask aperture is then measured between the two equal mass interfaces. As indicated in Fig. 5, the aperture size for the nominally 100 \AA Ge deposition is approximately $2.71 \mu\text{m}$. Because clogging of the aperture can be expected, a clogging factor of $1/4$ of the deposition thickness times 2, for the two edges, is used to correct the aperture size for each deposition. This factor of $1/4$ was measured for Al from cross-sectional SEM measurements of the masks, and this factor was applied to all elements in this study. The total correction is small; for example, during the Al, Ti, Pt, Au, and Cr depositions, the aperture size is decreased by only $0.06 \mu\text{m}$.

To quantify the lateral diffusion length for a given deposition, the difference between the full width at half maximum of the deposited feature and the mask aperture size is computed. This diffusion length is extracted for each structure and plotted as a function of the square root of time in Fig. 6. Elements that were deposited first had the longest diffusion time and elements deposited last received the shortest diffusion. The order of depositions can be read from right to left. The diffusion length shows an approximately linear dependence on the square root of time as expected for Fick's law of diffusion and this diffusion appears to be roughly independent of the element. Since two Al deposition sequences were performed, the diffusion coefficient of Al on SiO_2 , D_{Al} , can be estimated from $L = \sqrt{D_{\text{Al}}t}$, where t is the diffusion time. The line fitted to the Al data points is shown in Fig. 6 with the corresponding diffusion coefficient of $6.7 \times 10^{-14} \text{ cm}^2/\text{s}$.

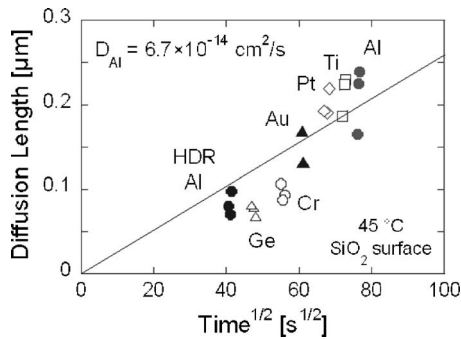


FIG. 6. Lateral diffusion length vs square root of the annealing time and vs deposited element in vacuum on SiO_2 at 45°C .

A linear fit using all data points gives a diffusion coefficient that is only 5% less than D_{Al} . Reported values for D_{Al} at similar temperatures vary from 6.4×10^{-15} (Ref. 10) and 7.2×10^{-12} cm^2/s at 45°C (Ref. 11) in good agreement with this result. Also of note in Fig. 6 is that for each element three different thicknesses were deposited giving rise to the three points per element shown. A difference between the diffusion length and thickness of the deposition can be seen which is not explained by Fick's law of diffusion. This dependence of lateral spread on the deposited layer thickness is an evidence of a second diffusion mechanism.

This second mechanism is consistent with the following model. First, the sticking probability of the impinging molecules is assumed to be unity, since near room temperature desorption is negligible.¹² Second, adatoms reaching the oxide surface are in a mobile, weakly adsorbed state,^{11,13,14} with the first monolayer of atoms becoming immobilized by bonding with the oxide surface. Adatoms landing on this first monolayer remain in the mobile state and diffuse to an energetically favorable step edge, increasing the lateral size of the layer, or contribute to the thickening of the film by forming new stable islands after colliding with other atoms. Adatoms landing close to the aperture edge have a higher probability of diffusing into the shadow region, and since this region does not receive an impingement flux, adatoms are less likely to be immobilized by other atoms. Thicker depositions provide more adatoms for diffusion under the mask and produce larger halos. The formation of Al microcrystals away from the deposition edge is surprising and not explained by this model.

We define the halo extent as the difference between the geometrical deposition edge and the maximum observable edge of the halo from the top view AFM images in Fig. 2. Shown in Fig. 7(a) is a comparison of the halo extent versus the deposition thickness for each deposited film. The error bars represent the uncertainty in selecting the edges. This uncertainty varies for each deposition and depends both on the element and on the quality of the image. The lower error bar indicates the minimum possible dimension, the upper error bar, the maximum dimension, and the data symbols, the most likely edge positions. The halo extent correlates both with the deposition thickness and with the time at 45°C . With the exception of the HDR Al, the longer the time, the

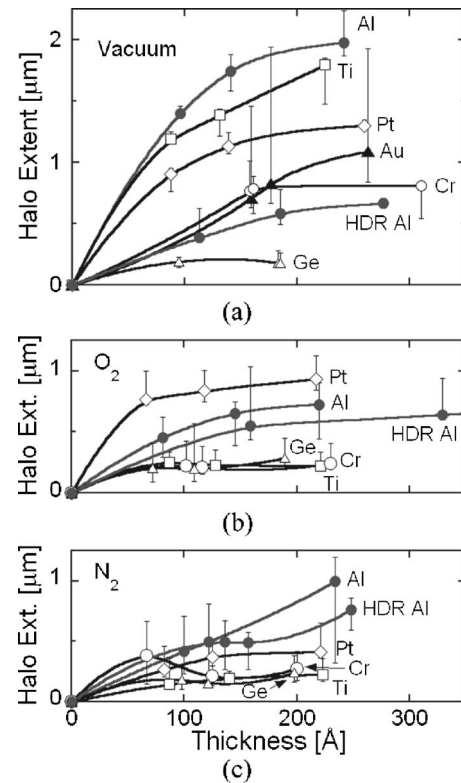


FIG. 7. Halo extent (distance from deposition edge to edge of halo) vs deposition thickness for materials deposited on SiO_2 at 45°C : (a) in vacuum at 1.8×10^{-6} Torr, (b) with oxygen background pressure of 5×10^{-5} Torr, and (c) with nitrogen background pressure of 5×10^{-5} Torr.

greater the halo extent. Increasing the Al deposition rate by approximately $3 \times$ in the HDR Al deposition decreases the extent of the halo by approximately $4 \times$. This is consistent with the idea that higher deposition fluxes lower the surface mobility, enhance the nucleation of islands, and provide fewer adatoms to the regions shadowed by the stencil mask. The greatest halo extent is seen for Ti, Al, Pt, and Au [Fig. 7(a)] which all spread out over one micron. The halo for Ge is significantly less but still can exceed $0.1 \mu\text{m}$. There appears to be a saturating trend to the halo extent which is consistent with the idea that the edge growth decreases as the edge moves away from the aperture opening.

Diffusion can be suppressed by lowering the substrate temperature. Deshmukh *et al.*¹ reported that vacuum deposition onto a substrate cooled to liquid nitrogen temperature decreased the spreading of Er dots on SiO_2 by a factor of 2 compared to room temperature. Surface diffusion can also be suppressed by deposition in a mobility-inhibiting gas ambient.^{15–17} Oxygen pressures of 10^{-4} – 10^{-5} Torr decrease the mobility of deposited atoms¹⁵ by either forming an oxide layer that prevents diffusion¹⁶ or by being incorporated into the layer interstitially.¹⁷ Chopra¹⁵ shows that some gases (e.g., O_2 or N_2) adsorb epitaxially and may increase the desorption energy of surface adatoms, thus, decreasing their mobility.

A repeat of these experiments was performed in O_2 and N_2 ambients to see if surface diffusion could be retarded, and

these results are plotted in Figs. 7(b) and 7(c). A pressure of 50 μ Torr was selected. At this pressure and for a deposition rate of 10 $\text{\AA}/\text{s}$ the ratio of gas molecules striking the substrate versus metal atoms adhering to the substrate is approximately 3:1, as can be calculated from the monolayer formation time of gas molecules.¹⁸ Thus, at this pressure and deposition flux there are comparable numbers of gas molecules and deposited atoms available for reaction and incorporation. The decrease in the halo extent for depositions in O_2 and N_2 is apparent in Figs. 7(b) and 7(c), respectively. For all the metals the extent of the halo was reduced at the higher pressure in both ambients by a factor ranging from approximately 2 to 8. In the vacuum experiments it was observed that in the case of Au, instead of continuous layers, microcrystalline islands form on the surface. The presence of these scattered islands made the measurement of the extent of the halo and the thickness of the deposit too uncertain to include in the plots of Figs. 7(b) and 7(c). The halo extent of Ti and Cr became comparable to Ge on evaporation in the gas ambient. The changes in the already low surface diffusion of Ge and HDR Al were small and within the error of the measurement.

The decrease in surface diffusion in O_2 and N_2 ambients is consistent with the following physical description. Gas molecules immobilize adatoms by either forming a chemical bond or providing a surface diffusion barrier in the diffusion path of a mobile adatom. For the HDR Al, the halo extent is not significantly altered by the 50 μ Torr gas ambient; in this case the ratio of mobility-inhibiting gas molecules striking the surface is not high enough to significantly influence the adatom movement.

V. CONCLUSIONS

Translated stencil masks have been used to deposit and compare the lateral diffusion of Al, Au, Cr, Ge, Pt, and Ti on SiO_2 near room temperature. The motion of the deposition edge of a film deposited through an aperture appears to be consistent with Fick's law of diffusion, however, the movement of the deposition edge out under the stencil mask as the deposition thickness increases suggests that the thicker film

is feeding more adatoms into the region shadowed by the mask. Increasing the deposition rate of the deposited material retards the motion of the material into the shadow region by decreasing the adatom surface mobility. By performing depositions in O_2 and N_2 ambients, the lateral motion was shown to be suppressed by a factor typically more than 2 and as much as $(7-8)\times$.

ACKNOWLEDGMENTS

This material is based upon the work supported by the National Science Foundation under Grant No. 0420957. The research was also aided by the work of John Timler, under the DCI Postdoctoral Research Fellowship Program. The authors would like to thank T. Kosel and A. Miller for helpful discussions and suggestions, K. Darr for his assistance with modifications of the vacuum system, and also J. Timler for the development of the closed-loop temperature control.

- ¹M. M. Deshmukh, D. C. Ralph, M. Thomas, and J. Silcox, *Appl. Phys. Lett.* **75**, 1631 (1999).
- ²R. Lüthi, R. R. Schlittler, J. Brugger, P. Vettiger, M. E. Welland, and J. K. Gimzewski, *Appl. Phys. Lett.* **75**, 1314 (1999).
- ³Z. Rácz *et al.*, *J. Vac. Sci. Technol. B* **22**, 74 (2004).
- ⁴A. R. Champagne, A. J. Couture, F. Kuemmeth, and D. C. Ralph, *Appl. Phys. Lett.* **82**, 1111 (2003).
- ⁵S. Egger, A. Ilie, Y. Fu, J. Chongsathien, D. J. Kang, and M. E. Welland, *Nano Lett.* **5**, 15 (2005).
- ⁶B. Voigtländer and M. Kästner, *Surf. Sci.* **464**, 131 (2000).
- ⁷L. L. Levenson, A. B. Swartzlander, A. Yahashi, H. Usui, and I. Yamada, *Scanning Microsc.* **5**, 679 (1991).
- ⁸V. Blech, T. Nobuyuki, and B. Kim, *J. Vac. Sci. Technol. B* **24**, 1 (2006).
- ⁹P. Shewmon, *Diffusion in Solids*, 2nd ed. (The Minerals, Metals, and Materials Society, Warrendale, PA, 1989), p. 36.
- ¹⁰F. Y. Génin, *J. Appl. Phys.* **77**, 5130 (1995).
- ¹¹T. S. Cale, M. K. Jain, D. S. Taylor, R. L. Duffin, and C. J. Tracy, *J. Vac. Sci. Technol. B* **11**, 2 (1993).
- ¹²M. Bäumer and H.-J. Freund, *Prog. Surf. Sci.* **61**, 127 (1999).
- ¹³G. Raynerd, M. Hardiman, and J. A. Venables, *Phys. Rev. B* **44**, 13803 (1991).
- ¹⁴J. A. Thornton, *Annu. Rev. Mater. Sci.* **7**, 239 (1977).
- ¹⁵K. L. Chopra, *Thin Film Phenomena* (McGraw-Hill, New York, 1969), p. 230.
- ¹⁶H. L. Caswell and Y. Budo, *J. Appl. Phys.* **35**, 644 (1964).
- ¹⁷H. L. Caswell, *J. Appl. Phys.* **32**, 2641 (1961).
- ¹⁸M. Ohring, *The Materials Science of Thin Films* (Academic, Boston, 1992), p. 54.